Journal of the Meteorological Society of Japan, Vol. 95, No. 5, pp. 301−317, 2017
DOI:10.2151/jmsj.2017-017

Feasibility Study for Future Space-Borne Coherent Doppler Wind Lidar, Part 1: Instrumental Overview for Global Wind Profile Observation

Shoken ISHII, Philippe BARON, Makoto AOKI, Kohei MIZUTANI, Motoaki YASUI, Satoshi OCHIAI

Applied Electromagnetic Research Institute, National Institute of Information and Communications Technology, Koganei, Japan

Atsushi SATO

Graduate Department of Environmental Information Engineering, Tohoku Institute of Technology, Sendai, Japan
National Institute of Information and Communications Technology, Koganei, Japan

Yohei SATOH, Takuji KUBOTA, Daisuke SAKAIZAWA, Riko OKI

Japan Aerospace Exploration Agency, Tsukuba, Japan

Kozo OKAMOTO

Meteorological Research Institute, Japan Meteorological Agency, Tsukuba, Japan
National Institute of Information and Communications Technology, Koganei, Japan

Toshiyuki ISHIBASHI, Taichu Y. TANAKA, Tsuyoshi T. SEKIYAMA, Takashi MAKI

Meteorological Research Institute, Japan Meteorological Agency, Tsukuba, Japan

Koji YAMASHITA[1]

Numerical Prediction Division, Japan Meteorological Agency, Chiyoda, Japan

Tomoaki NISHIZAWA

Atmospheric Environment Division, National Institute for Environmental Studies, Tsukuba, Japan

Masaki SATOH

Atmosphere and Ocean Research Institute, The University of Tokyo, Tokyo, Japan

Corresponding author: Shoken Ishii, National Institute of Information and Communications Technology, 4-2-1 Nukuikita-machi, Koganei-shi, Tokyo 184-8795, Japan
E-mail: sishii@nict.go.jp
[1] Present affiliation: Meteorological Satellite Center of Japan Meteorological Agency, Tokyo, Japan
J-stage Advance Published Date: 19 June 2017

and

Toshiki IWASAKI

Graduate School of Science, Tohoku University, Sendai, Japan

(Manuscript received 2 May 2016, in final form 6 June 2017)

Abstract

A working group is studying the feasibility of a future Japanese space-borne coherent Doppler wind lidar (CDWL) for global wind profile observation. This study is composed of two companion papers: an instrumental overview of the space-borne CDWL for global wind profile observation (Part 1), and the wind measurement performance (error and bias) investigated using a full-fledged space-borne CDWL simulator (Part 2). This paper aims to describe the future space-borne CDWL in terms of technical points and observation user requirements. The future mission concept is designed to have two looks for vector wind measurement with vertical resolutions of 0.5 (lower troposphere: 0–3 km), 1 (middle troposphere: 3–8 km), and 2 km (upper troposphere: 8–20 km) and horizontal resolution of < 100 km along a satellite. The altitude and orbit of the satellite are discussed from a scientific viewpoint. The candidate altitude and orbit of the satellite are 220 km and an inclination angle of 96.4° (polar orbit) or 35.1° (low-inclination-angle orbit). The technical requirements of the space-borne CDWL are a single-frequency 2-μm pulse laser with an average laser power of 3.75 W, two effective 40-cm-diameter afocal telescopes, a wide-bandwidth (> 3.4 GHz) detector, a high-speed analog-to-digital converter, and a systematic lidar efficiency of 0.08. The space-borne CDWL looks at two locations at a nadir angle of 35° at two azimuth angles of 45° and 135° (225° and 315°) along the satellite track. The future space-borne CDWL wind profile observation will fill the gap of the current global wind observing systems and contribute to the improvement of the initial conditions for numerical weather prediction (NWP), the prediction of typhoons and heavy rain, and various meteorological studies.

Keywords Doppler wind lidar; Earth observation satellite; global wind profile observation; numerical weather prediction; lidar simulator; observing system simulation experiment

1. Introduction

Severe weather-related disasters are becoming increasingly serious in many parts of the world, and people are in danger more than ever because of weather-related disasters and climate change. Improvements in numerical weather prediction (NWP) are important for disaster prevention or disaster risk reduction. Wind is one of the fundamental meteorological variables describing the atmospheric state (pressure, temperature, and humidity). Global wind profile observation is crucial to significantly improve the initial conditions essential for global and regional NWP, air quality forecasts, climate studies, and various meteorological studies. The World Meteorological Organization (WMO) organizes various observing networks and systems to provide a wide range of meteorological descriptions. WMO has many scientific and technical programs to solve present and future problems. Current space-borne observing systems are biased toward temperature- and water-vapor-related measurements in comparison with wind measurements (Baker et al. 2014). The WMO Integrated Global Observing System technical report (WMO 2012) states, "Development of satellite-based wind profiling systems remains a priority for the future global observing system". Tables 1a and 1b show current user requirements of wind profile observation for global NWP (WMO 2015, http://www.wmo-sat.info/oscar/variables/view/179) and a summary of current global wind observing systems, respectively. While these requirements are for globally homogeneous wind profile observation, current global wind observing systems do not always satisfy these requirements. Automatic weather station networks, buoy networks, and ships provide surface meteorological information with a large coverage but provide few meteorological profiles. Ground-based wind profilers provide wind profiles, but such wind profilers are installed only in Japan, Western Europe, and North America. Wind profiles are mainly provided by radio-

Table 1. (a) Ideal (Goal), breakthrough (BT), and threshold (TH) observational user requirements of wind profiling observation for global numerical weather prediction: lower troposphere, upper troposphere, and lower stratosphere.

Target atmosphere	Vertical resolution (km)			Horizontal resolution (km)			Wind accuracy (m s^{-1})			Observing cycle (h)			Delay of availability (h)		
	Goal	BT	TH	Goal	BT	TH	Goal	BT	TH	Goal	BT	TH	Goal	BT	TH
Lower troposphere (LT)									5						
Upper troposphere (UT)	0.5	1	3	15	100	500	1	3	8	1	6	12	0.1	0.5	6
Lower stratosphere (LS)									5						

(b) Summary of current global wind observing systems.

Instrument	Altitude (km)	Coverage	Observing cycle (hour $days^{-1}$)	Wind accuracy (m s^{-1})
Buoys and ships	Sea surface	Ocean	24/7	< 0.3
Auto weather station	Surface	Land	24/7	0.1
Wind profiler	Surface- 10	Land	24/7	1
Aircraft	Flight level	Mainly northern hemisphere land	24/7	1–3
Radiosonde	Surface- 30	Mainly northern hemisphere land	12 or 24/7	< 0.2
Space-borne microwave scatterometer/ radiometer	Sea surface	Ocean	24/7	2
Space-borne microwave imager (AMV)	Mainly cloud top	Land and ocean	3/7	Bias < 2, RMS > 4

sonde networks and by aircraft measurements. The radiosonde and aircraft measurements are mainly performed over populated regions in the northern hemisphere but not in the southern hemisphere. The number of weather stations observing the upper atmosphere has been decreasing. A lack of wind observation over oceans, the southern hemisphere, and other sparse areas causes nonuniform errors in NWP and their subsequent analysis. Single-layer vector wind can be measured by satellite-borne microwave scatterometers and polarimetric microwave radiometers, and multiple-layer vector wind, called the atmospheric motion vector (AMV), can be retrieved from cloud and water vapor motions derived from geostationary and polar-orbit satellite images. As discussed in our previous study (Ishii et al. 2016), the AMV achieves a large coverage area and high temporal and horizontal resolutions (2.5 and 10 min, 0.5° × 0.5°) but has a low vertical resolution (2–4 km). The bias and root-mean-square (RMS) vector difference of the AMV retrieval verified against radiosonde wind observations presented in previous studies (e.g., Hayashi and Shimoji 2013; Otsuka et al. 2015) are relatively large (bias of less than 2 m s^{-1} and RMS vector difference of worse than 4 m s^{-1}). The AMV can hardly retrieve vector winds under thick clouds, over dry regions, clear-sky regions or regions with few clouds, the atmosphere near Earth's surface over inland area, and low-wind-speed regions. The height assignment of the AMV remains very inaccurate, and it causes significant vector wind errors (RMS vector difference of 4–8 m s^{-1}) (Velden and Bedka 2009). There are 30–60 hPa differences in the height assignment between the AMV and other instruments (Velden and Bedka 2009; Folger and Weissmann 2014).

A Doppler wind lidar (DWL) provides us with a wind profile having high vertical resolution, low bias, and good precision, and it is necessary to fill the gap of current observations. The impacts of space-borne DWL wind observations on NWP have been assessed by OSSEs (Riishøjgaard et al. 2004; Stoffelen et al. 2005; Marseille et al. 2008; Masutani et al. 2010; Ishibashi 2014; Atlas et al. 2015a, b). The European Space Agency is planning to launch the first space-borne DWL called ADM-Aeolus for obtaining global wind profiles (ESA 1999; Stoffelen et al. 2005) in 2017 (https://earth.esa.int/web/guest/missions/esa-future-missions/adm-aeolus). ADM-Aeolus uses a single-frequency UV laser and a direct-detection system. ADM-Aeolus will provide profiles of a single line-of-sight (LOS) wind speed. In the United States, NOAA and NASA conducted several feasibility studies of

shuttle- and space-borne CDWLs (Huffaker 1978; Huffaker et al. 1980, 1984; Menzies 1986; Bilbro et al. 1987; NASA 1989; Petheram et al. 1989; Kavaya and Emmitt 1998). The Global Wind Observing System mission concept was proposed to the National Research Council (2007), which was planned to demonstrate the potential of wind vector measurements with a hybrid DWL (Emmitt 2001). The Winds from the International Space Station for Climate Research (WISSCR) mission study was conducted in late 2010 and early 2011 (Hardesty et al. 2011; Baker et al. 2014). The Optical Autocovariance Wind Lidar (OAWL) is composed of a 0.355-μm (or 0.532-μm) single-frequency laser and a direct-detection DWL with a Mach–Zehnder interferometer (Grund et al. 2009; Tucker and Weimer 2014). The OAWL measures signal intensities simultaneously at several fixed phase delays after passing the Mach–Zehnder interferometer and determines the optical autocovariance functions of the outgoing laser and backscattered signals. The phase difference between the two functions provides us the Doppler-shifted frequency, and then wind speed is given by the Doppler-shifted frequency.

In Japan, studies on the feasibility of the International Space Station (ISS)-borne coherent DWL (CDWL), called JEM-CDWL, were conducted in the late 1990s (Iwasaki 1999). NICT, Tohoku University, The University of Tokyo, Meteorological Research Institute (MRI), and JAXA organized a working group for a future Japanese space-borne CDWL in 2011 and are studying its feasibility from the technical and scientific viewpoints to enhance the feasibility of the space-borne CDWL. The space-borne CDWL is proposed to be carried on a super-low-altitude satellite (SLAS; Noda et al. 2009). The SLAS is a new satellite with ion-propulsion technologies being developed by JAXA, which will fly in a circular orbit at altitudes of 180−250 km. Because more fuel is needed to keep the satellite in the low orbital altitude from descending owing to atmospheric drag, the operation period of the SLAS may be limited. However, more importantly, the low orbital altitudes allow us to reduce the pulse energy of the laser, the diameter of the telescope, and the electrical power consumption required for space-borne active remote sensing systems, which is a promising approach for next-generation Earth observation satellites. The objectives of the future space-borne CDWL are to demonstrate multi-looking LOS wind profiling observations, the retrieval of vector wind, compensation techniques for the Doppler shift due to the satellite speed, and the advantages of Earth observation at low altitudes. Preliminary results of the measurement performances of a space-borne CDWL simulator and the concept of an OSSE study were described previously (Ishii et al. 2016). The latest results show that the percentage of wind profiling observations with good-quality estimates is 40 % below 8 km over the latitudes except for the equatorial region in the southern hemisphere and that the expected LOS wind speed error for good-quality estimates is 0.5 m s^{-1} below 8 km. The results of the OSSE study show that the forecast improvement rates for the wind speed at 850 hPa for a 36-h forecast are apparent, especially in the middle and high latitudes of the southern hemisphere. The results suggest that global wind profile observations could have additional positive impacts on the NWP system. This paper is composed of two companion papers. In Part 1, we provide an overview of global wind profiling observation and technical strategies for designing the space-borne CDWL. In Part 2, measurement performances using a space-borne lidar simulator will be discussed by characterizing the retrieved LOS wind speed and the LOS wind speed error and bias under various atmospheric conditions (Baron et al. 2017). As a future companion paper of Parts 1 and 2, full OSSEs will be discussed to determine the potential impacts of global wind profiles simulated using the space-borne CDWL simulator for NWP (Okamoto et al. 2017) in accordance with the flow shown in Fig. 1. This paper is arranged as follows. In the next section, we describe coherent and direct-detection DWL and wind measurement principle of a CDWL. The global wind profiling observation geometry of the space-borne CDWL is shown in Section 3. Key technologies required for the space-borne CDWL are described in Section 4. A summary of this paper is presented in Section 5.

2. Doppler wind lidar

2.1 Technical comparison of coherent and direct-detection Doppler wind lidar

DWL is an active remote sensing system providing wind profiles. Coherent- or direct-detection DWLs have been developed by research groups for a long time. A CDWL uses the Doppler-shifted frequency of infrared (IR) laser light backscattered mainly by coarse-mode aerosols (Mie scattering) (Seinfeld and Pandis 1988) moving with the wind. On the contrary, most of the direct-detection DWL types use ultraviolet (UV) laser light backscattered by small aerosols or molecules (Rayleigh scattering), or both types of scattering. Both IR and UV lasers are in the eye-safe region. The target atmosphere of a CDWL is the atmospheric boundary layer, lower troposphere, and middle

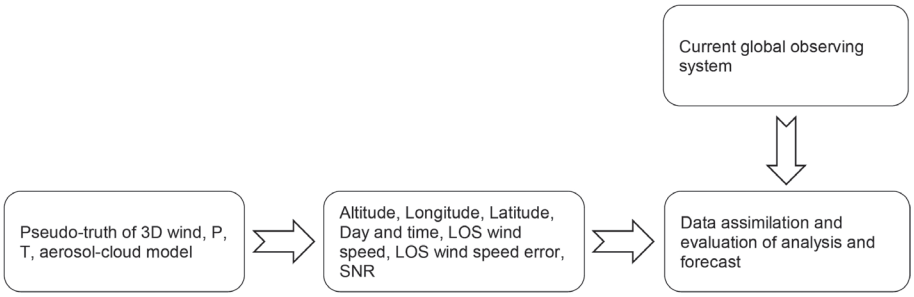

Fig. 1. Numerical simulation flow from space-borne CDWL lidar simulator to OSSE.

troposphere due to dependence on aerosol abundances. A direct-detection DWL is used for tropospheric wind measurement with the Mie and/or Rayleigh scattering and stratospheric wind measurement with the Rayleigh scattering. The development of an IR laser capable of meeting the requirements of a space-borne DWL system is technically feasible (Sato et al. 2017). Nd:YAG lasers are a matured laser technology. There are many challenges (e.g., laser-induced damage, contamination) in developing a space-qualified UV laser meeting the requirements of a space-borne DWL. Such instrument with an average laser power of 5 W has not yet been achieved in Japan. In a CDWL, a coaxial configuration is employed, while in a direct-detection DWL both coaxial and biaxial configurations are employed. In a CDWL, a portion of a single-frequency continuous-wave laser beam described in Section 2 must be matched with the backscattered light beam to maximize the signal-to-noise ratio (SNR), which means that a CDWL uses a receiver with a very narrow bandpass. A CDWL can be used to make daytime and nighttime wind measurements. A direct-detection DWL uses an m-class diameter and a lightweight telescope with a narrow field of view, an interferometer (e.g., Fabry–Pérot etalon, Mach–Zehnder), and narrowband optical bandpass filters to maximize the SNR by reducing the background radiation. Although a direct-detection DWL also performs nighttime and daytime wind measurement, the use of the narrowband optical bandpass filters in the daytime measurement results in the degradation of observable range due to the decrease of backscattered signal. The diameter of the telescope is limited by the size of the spacecraft. A CDWL does not require such a large-area telescope. A CDWL can directly measure a Doppler-shifted frequency without bias (in principle) and with random wind error better than 1 m s^{-1} (Ishii et al. 2010; Iwai et al. 2013; Baron et al. 2017). The precision of CDWL wind measurement depends on the aerosol abundance and speckle (Rye 1979; Frehlich and Kavaya 1991). Speckle has temporal and spatial components, and it is considered in heterodyne efficiency. The performance of direct-detection DWL required for space-borne DWL wind measurement has a bias of 0.4 m s^{-1} and a precision of 0.6–1.7 m s^{-1} (ESA 2001). It depends on the sensitivity curve of the receiver for wind speed. It is very important to make bias-free wind measurements with high precision, especially for NWP over a weak wind region or for comparison and validation with the AMV. There are sinks and sources of various substances in the lower troposphere. Wind measurement with low bias and high precision is also necessary for estimating the flux of materials. For a future SLAS mission, the CDWL was selected as result of many considerations (difficulties of using UV laser, diameter of telescope, bias and precision, and so on). A comparison of the SLAS-borne CDWL and space-borne direct-detection DWL is summarized in Table 2.

2.2 Principle of coherent Doppler wind Lidar

The basic principle of a CDWL is described in Fig. 2, which is similar to that of a Doppler radar, but not the same. The basic components of the CDWL are a single-frequency continuous-wave (CW) laser, a pulse laser, a telescope, two heterodyne detectors, optical components, and signal processing components. The single-frequency CW laser passes through an acoustic optical modulator (AOM), and the AOM shifts the frequency of the single-frequency CW laser. The frequency-shifted CW laser is used for both injection seeding to achieve a single-frequency pulse laser and heterodyne detection. The single-frequency laser pulses are sent into the atmosphere at a nadir angle. The backscattering coefficient of atmospheric molecules (Rayleigh scattering) is inversely proportional

Table 2. Comparison of SLAS-borne CDWL and space-borne direct-detection DWL. SWIR, UV, and VIS denote short-wavelength infrared, ultraviolet, and visible, respectively.

	SLAS-borne CDWL	Direct-detection DWL
Observable time zone	Daytime and nighttime	Daytime and nighttime
Target atmosphere	Lower troposphere	Troposphere, lower stratosphere
Scattering	Aerosol	Aerosol, Molecular
Wavelength band	SWIR	UV
Laser average power	2.5 W class	5 W$^{(**)}$ class, (30 W$^{(***)}$ class)
Telescope size	Middle (0.5 m)	Large (1–1.5$^{(**)}$ m)
Detection technique	Heterodyne (optical mixing)	Optical frequency discriminator Spectrum analyzer
Accuracy	Bias-free in principle, (0.0 m s^{-1})	Significant bias, (0.4 m s$^{-1(**, ****)}$)
Precision	0.1–1 m s$^{-1(*)}$	0.6–1.7 m s$^{-1(**)}$

* Dependence on aerosol abundance and speckle. ** European mission (ADM-Aeolus).
*** Future US mission. **** Dependence on atmospheric conditions and systematic bias.

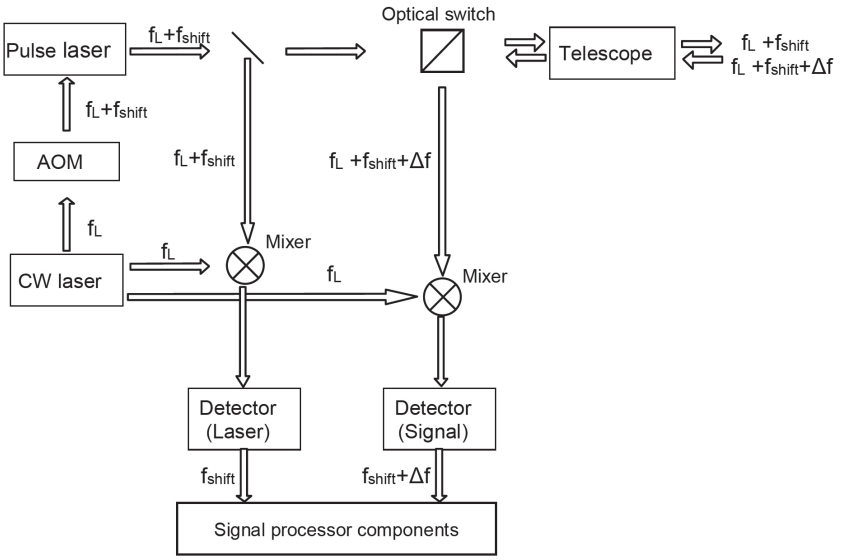

Fig. 2. Principle and basic components of CDWL. f_L is laser frequency. f_{shift} is shifted frequency modulated by an optical device. Δf is Doppler-shifted frequency. $\Delta f = (f_{\text{shift}} + \Delta f) - f_{\text{shift}}$. Two mixers are used to mix a single-frequency CW laser beam with an outgoing laser beam and backscattered light.

to the fourth power of the wavelength. In the 2-μm region, the backscattering coefficient of atmospheric molecules is negligible relative to that of aerosols. The backscattering coefficient of aerosols (Mie scattering) is assumed to depend on the wavelength with a power law of a negative Ångström exponent (Ångström 1964), where the Ångström exponent is related to the size distribution of aerosols. The Ångström exponent at the 2-μm region is approximately 0.3 to 2 (Srivastava et al. 2001). The CDWL mainly detects signals backscattered by moving aerosol particles to measure the Doppler-shift frequency of the LOS wind speed. A portion of the nonfrequency-shifted single-frequency CW laser is photomixed with the frequency-shifted CW laser on one detector and with the backscattered signals on the other detector. Each detector converts the frequencies of the outgoing laser and backscattered signals down to an intermediate frequency (IF). The detection process is called heterodyne detection. In general, the heterodyne detection is performed under a shot-noise-limited condition where the detector noise due to the non-frequency-shifted single-frequency CW laser power dominates all other noise. The IFs of the two signals are determined by frequency analysis.

The Doppler-shifted frequency Δf is then given as the difference frequency between the mean IFs of the two signals: $\Delta f = (f_L + f_{\text{shift}} + \Delta f) - (f_L + f_{\text{shift}})$. The Doppler-shifted frequency directly determines the LOS wind speed of a vector wind. The LOS wind speed V_{LOS} is obtained as

$$V_{\text{LOS}} = \frac{\lambda_L}{2} \cdot \Delta f, \tag{1}$$

where λ_L is the laser wavelength. At a λ_L of 2 μm, Δf of 1 MHz corresponds to an LOS wind speed of 1 m s^{-1}. The LOS wind speed depends on the vector wind components u, v, and w. V_{LOS} is given by

$$V_{\text{LOS}} = u \cdot \sin\theta_{\text{LOS}} \cdot \sin\varphi_{\text{LOS}} + v \cdot \cos\theta_{\text{LOS}} \cdot \sin\varphi_{\text{LOS}} + w \cdot \cos\varphi_{\text{LOS}}, \tag{2}$$

where θ_{LOS} is the azimuth angle from north and φ_{LOS} is the nadir angle of the laser beam.

The effective number of coherent signal photons Φ detected per range gate ($\Delta r = c \cdot MT_s/2$) per shot for target range r (m) is given as (Frehlich 2004)

$$\Phi = \eta_Q \cdot \eta_H \cdot \eta_O \cdot E_T \cdot \frac{A_R}{r^2} \cdot \beta(r) \cdot T_R{}^2 \cdot \frac{\Delta r}{hf_L}, \tag{3}$$

where $c = 2.998 \times 10^{-8}$ is the light speed (m s^{-1}), M is the number of sampling points, and T_S is the sampling interval (s). η_Q, η_H, and η_O are the quantum efficiency of the detector, the heterodyne efficiency, and the optical efficiency, respectively. E_T is the pulse energy of the laser (J pulse^{-1}), A_R is the telescope area (m^2), $\beta(r)$ is the backscattering coefficient of the target atmosphere (m^{-1} sr^{-1}), $T_R(r)$ is the one-way transmission between the lidar and the target atmosphere, and $h = 6.626 \times 10^{-34}$ (J s) is Planck's constant.

The optical signal current $I_S(t)$ (A) on a linear detector is expressed as (Frehlich and Kavaya 1991)

$$I_S(t) = I_{DC}(t) + I_S(t) + I_{DK}(t) + I_T(t) + i_{IF}(t), \tag{4}$$

where $I_{DC}(t)$, $I_S(t)$, $I_{DK}(t)$, $I_T(t)$, and $i_{IF}(t)$ are the direct current (A) caused by the single-frequency CW laser, the direct-detection signal current caused by the backscattered signal (A), the dark current (A), the thermal noise current (A), and the IF signal current (A), respectively. $I_{DC}(t)$ and $I_S(t)$ are expressed as

$$I_{DC}(t) = G \cdot \frac{\eta_Q e}{hf_L} \cdot P_{\text{Single-frequency CW laser}}, \tag{5}$$

$$I_S(t) = G \cdot \frac{\eta_Q e}{hf_L} \cdot P_{\text{Direct-detection signal}}, \tag{6}$$

where G is the amplifier gain (dimensionless), $P_{\text{Single-frequency CW laser}}$ and $P_{\text{Direct-detection signal}}$ current are the single-frequency CW laser power (W) and the direct-detection signal power current (W), respectively, and $e = 1.602 \times 10^{-19}$ (C electron^{-1}) is the electronic charge. $P_{\text{Direct-detection signal current}}$ is expressed as the following equation using Φ:

$$P_{\text{Direct-detection signal}} = \frac{hf_L}{\eta_H MT_S}\Phi. \tag{7}$$

If the signal current $i_{IF}(t)$ for a homogeneous range gate (Δr) with a constant SNR and stationary wind is expressed as the discrete time series of backscattered signals (Zrnic 1979; Rye and Hardesty 1993; Frehlich and Yadlowsky 1994), $i_{IF}(t)$ is expressed as

$$i_{IF} = \sqrt{2\left(\frac{Ge}{hf_L}\right)^2 \eta_H \eta_Q \cdot P_{\text{Single-frequency CW laser}} \cdot P_{\text{Direct-detection signal}}} \cdot \sum_{k=-M}^{M} \exp\left(-2\pi^2 (w \cdot kT_s)^2 + i\frac{4\pi (f_{\text{shift}} + \Delta f) \cdot T_s}{\lambda_L}\right), \tag{8}$$

where w is the spectral width of the backscattered signal (Hz). The wideband SNR of the CDWL is the ratio of the average signal power to the average noise power and defined as

$$\text{SNR} = \frac{\langle i_{IF}(t)^2 \rangle}{\langle i_{DC}(t)^2 + i_S(t)^2 + i_{DK}(t)^2 + i_T(t)^2 \rangle}, \tag{9}$$

where $\langle\rangle$ denotes the ensemble average over time. We assume that the average noise powers, $\langle i_{DC}(t)^2 \rangle$ and $\langle i_S(t)^2 \rangle$, caused by the single-frequency CW laser and the backscattered signal, respectively, obey the Poisson statistics. $\langle i_{DC}(t)^2 \rangle$, $\langle i_S(t)^2 \rangle$, $\langle i_{DK}(t)^2 \rangle$, and $\langle i_S(t)^2 \rangle$ are expressed as

$$\langle i_{DC}(t)^2 \rangle = 2GeB\langle I_{DC} \rangle = 2G^2 e^2 B \frac{\eta_Q}{hf_L} \langle P_{\text{Single-frequency CW laser}} \rangle, \tag{10}$$

$$\left\langle i_S(t)^2 \right\rangle = 2GeB\langle I_S \rangle = 2G^2e^2B\frac{\eta_Q}{hf_L}\left\langle P_{\text{Direct-detection signal}} \right\rangle, \quad (11)$$

$$\left\langle i_D(t)^2 \right\rangle = 2GeB\langle I_D \rangle, \quad (12)$$

$$\left\langle i_{DK}(t)^2 \right\rangle = \frac{4K_B \cdot T_e \cdot B}{R_L}, \quad (13)$$

where B (Hz) is the bandwidth of the detector and amplifier, $K_B = 1.38054 \times 10^{-23}$ (J K^{-1}) is Boltzmann's constant, T_e (K) is the absolute temperature of the detector, and R_L (Ω) is the load resister of the detector. We substitute Eqs. (10)–(13) into Eq. (9). For a typical CDWL, the shot noise power due to the single-frequency CW laser power is much larger than all other noise powers, which is called the "shot-noise-limited condition". Then, the SNR is expressed as

$$\text{SNR} = \frac{\eta_H}{hf_L B}\left\langle P_{\text{Direct-detection signal}} \right\rangle. \quad (14)$$

The relation SNR = Φ/M' (M' = M/2) is for real number time series (Frehlich et al. 1997).

The theoretical lowest LOS wind speed error (dv) (m s^{-1}) is given by the Cramer–Rao lower bound (CRLB) (Scharf 1991; Rye and Hardesty 1993):

$$dv_{\text{CRLB},K} = \frac{\lambda_L \cdot F_S}{2}\sqrt{\frac{f_2^{\,2}}{K \cdot M}\left[\int_{-0.5}^{0.5}\frac{(f/f_2)^2}{\left\{1+\left(\frac{\text{SNR}}{\sqrt{2\pi}f_2}e^{-f^2/(2f_2^{\,2})}\right)^{-1}\right\}^2}df\right]^{-1}}, \quad (15)$$

where f_2 is the spectral width normalized by the sampling frequency F_S (Hz), and K is the number of accumulated pulses. f_2 is given by the spectrum width of the laser for the homogeneous atmosphere. Note that the CRLB in Eq. (15) is for complex number time series signal $\sqrt{2}$ smaller than for the real number time series signal. Using the nadir angle φ, the theoretical horizontal LOS wind error per range gate becomes $dv_{\text{HLOS}} = dv/\sin\varphi$. When we use the same algorithm as that of Part 2 to make wind retrieval of the CDWL data (Baron et al. 2017), $dv_{K=1}$ for a single pulse (K = 1) and SNR < 1 follows that the CLRB is approximately proportional to 1/SNR:

$$dv_{\text{CRLB},K=1} \propto 1/\text{SNR}. \quad (16)$$

Typically, SNR for good wind retrieval at 2 μm and at a height of 200 km is in the range between 10^{-3} and 10^{-2} (Baron et al. 2017). We assume that dv is independent random variable with a Gauss distribution. dv_{CRLB} for K pulses is given as

$$dv_{\text{CRLB},K} \propto 1/\left(\sqrt{K}\cdot\text{SNR}\right). \quad (17)$$

Using Eqs. (14), (16), and (17), and pulse repetition frequency (PRF) instead of K, we have $\sqrt{\text{PRF}}\cdot E_T$ = constant.

3. Global wind profiling observation geometry

The altitude and orbit (inclination, period) of a satellite are key parameters for studying the performances of space-borne remote sensing. Electric power, mass, and volume are also key parameters for designing the structure of a satellite, the size of a solar array panel, and the size of a radiator. In general, the observation altitudes of Earth observation satellites are in the range of 400–700 km. A polar-orbit satellite and the ISS fly in a circular orbit at an altitude of 400 km at inclination angles of 98° and 52°, respectively. The light power detected by a lidar is proportional to the pulse energy of the laser, the area of the receiver (telescope), and the optical efficiency, which is inversely proportional to the square of the distance between the lidar and the target atmosphere as described in Eq. (3). If the orbital altitude of a future candidate satellite were half that of the ISS, the pulse energy of the laser or the diameter of the telescope would be four times smaller. The target orbital altitude of the future SLAS is 220 km, which means that the pulse energy meeting the requirements of future space-borne CDWL would be four times smaller than that of the ISS-borne CDWL. The target design life of this satellite is 5 years owing to the fuel of the ion engine, and the target operation of the space-borne CDWL observation is 3–5 years. We are considering two candidate orbits for the future space-borne DWL: a sun-synchronous polar orbit (96.4°) and a low-inclination-angle orbit (35.1°). The electrical power consumption for maintaining the bus and running the sensor depends on the size of the solar array panel (SAP), the angle of cant of the

SAP, and the inclination angle of the SLAS. Detailed considerations are necessary for choosing the size and designing the structure of the SAP. Figure 3 shows the sun-synchronous polar and low-inclination-angle orbits. A comparison of the platform parameters for the future space-borne CDWL, ISS-borne JEM-CDWL, and ADM- Aeolus is summarized in Table 3.

Figure 4 shows the relation between the horizontal line-of-sight (HLOS) wind speed error and the nadir angle for various altitudes (surface, 2, 5, 8, and 10 km) and for the configuration depicted in Fig. 4. The HLOS wind speed error is calculated using Eqs. (3), (7), (14), and (15), the nadir angle, the enhanced aerosol model of the target atmosphere based on Global Backscatter Experiment (Bowdle et al. 1991) for use in the 2-μm CDWL concept study (http://www.swa.com/target-atmosphere-profiles), and the parameters described in a previous study (Ishii 2009, personal communication). The HLOS wind speed error depends on the target range r and the sine of φ. The HLOS wind speed error depends on the SNR. In general, the HLOS wind speed error is low in the lower troposphere. Since the SNR is slightly higher at the altitude of 5 km than at 2 km, the HLOS wind speed error for 5 km is lower than that for 2 km. The HLOS wind speed error decreases from nadir angles of 20° to 30°, decreases slightly

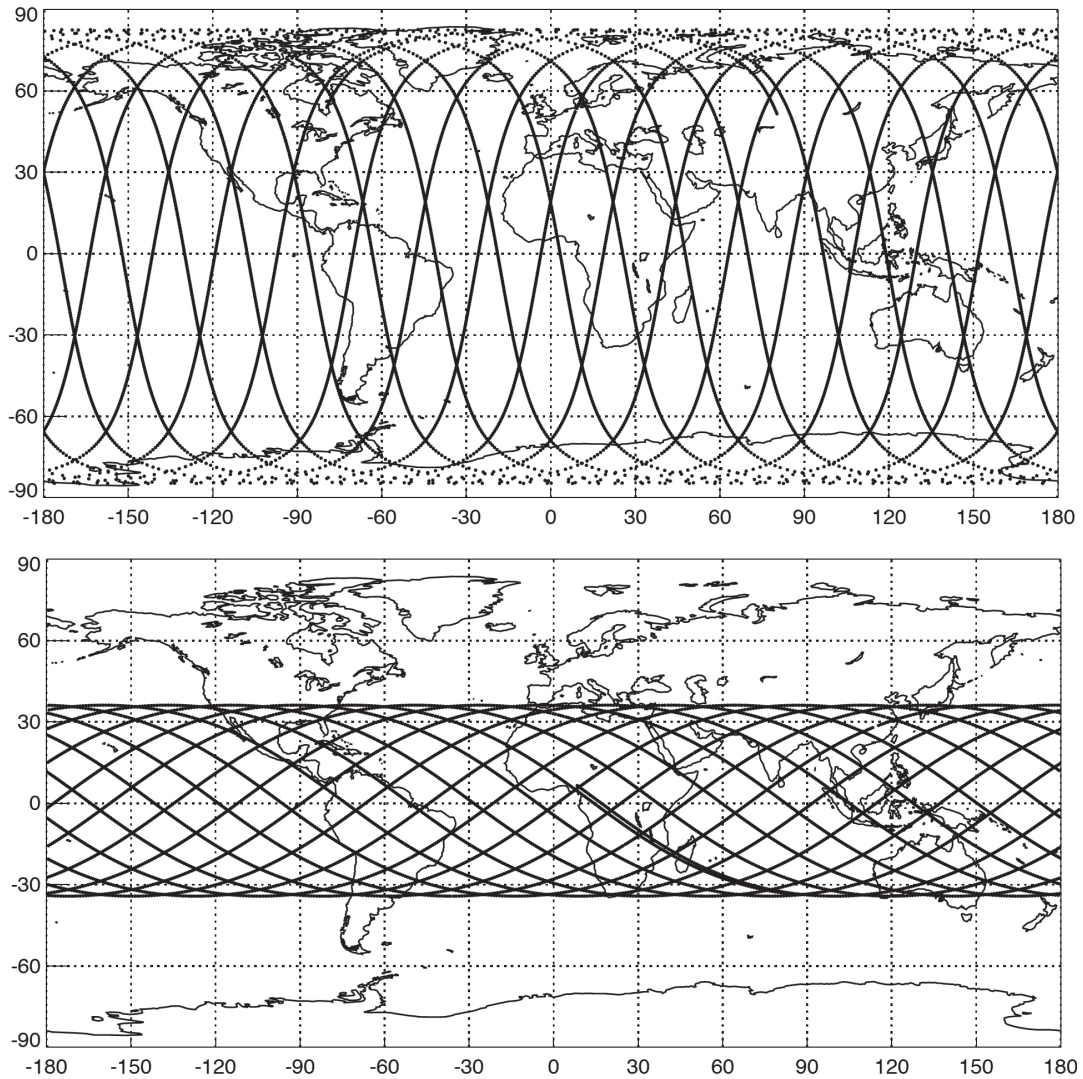

Fig. 3. Candidate orbit and coverage: (upper panel) sun-synchronous polar orbit and (lower panel) low-inclination-angle orbit.

Table 3. Comparison of platform parameters for SLAS-borne DWLs.

	SLAS-borne	ISS-borne JEM-CDL	ADM-Aeolus
Orbital altitude (km)	220	400	410
Orbital inclination (°)	96.4 (Polar, SSO) 35.1 (TRMM, non-SSO)	51.6 (non-SSO)	96.4 (SSO)
Orbital period (min)	89	93	93
Instrument volume (m^3)	1.5 × 1.0 × 1.0	1.8 × 1.0 × 0.8	4.3 × 1.9 × 2.0
Total / Instrument mass (kg)	$600^{(*)}$ / TBD	− / < 500	$1100^{(**)}$ / 470
Total / Instrument power (kW)	1600 / 730	− / 1250	1400 / 840

SLAS: super-low-altitude satellite. SSO: sun-synchronous orbit.
*: target total dry mass, **: total dry mass (not including fuel)

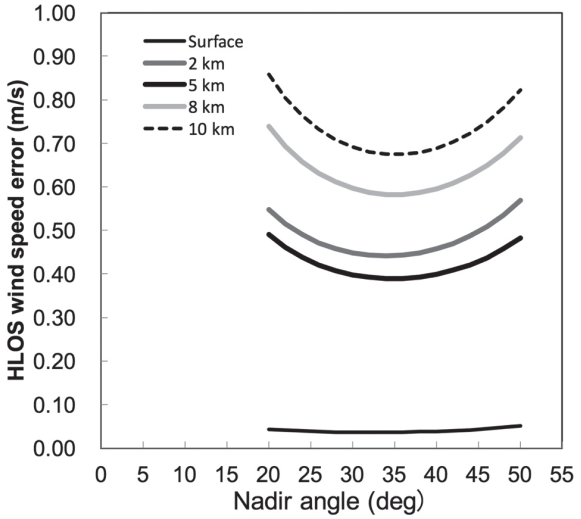

Fig. 4. Relation between nadir angle and horizontal line-of-sight (HLOS) wind speed error for various altitudes (surface, 2, 5, 8, and 10 km) for the configuration depicted in Fig. 5. The HLOS wind speed error is calculated using Eqs. (3), (7), (14), and (15), the nadir angle, and the enhanced aerosol model of the target atmospheres for use in DWL concept studies (Emmitt et al. 2001).

from 30° to 35°, and increases above 40°. The range between the lidar and the target atmosphere increases with the nadir angle, and the SNR decreases with the square of the target range. It is necessary to consider the horizontal resolution required by current users for wind profile observation. A nadir angle of 35° is selected for future space-borne CDWL observations. The horizontal wind direction is obtained by DWL observation of the same air mass from two directions (i.e., two LOS wind measurements). The LOS wind speed versus azimuth angle at the same altitude yields a sinusoidal curve. The LOS wind speed is 0 m s^{-1} for a laser beam direction perpendicular to the wind direction, and it is the maximum speed for a laser beam direction parallel to the wind direction. As the separation angle of the two laser beam directions decreases, the difference in the LOS wind speed decreases, which results in degradation of accuracy in vector wind measurement. Although the LOS azimuth angle relative to the satellite speed is fixed, the angle with respect to zonal or meridional components varies over 360° during a full orbit. However, the zonal or meridional components of the winds can be constructed from any LOS orientations since the two LOS are always perpendicular. When the two laser beams are projected onto a horizontal plane, the optimum configuration for reconstructing the wind vector is when both LOS are perpendicular. Azimuth angles of 45° (forward) and 135° (backward) (or 225° and 315°) are selected for vector wind measurement to the right of the orbit ground track (0° is the satellite flight direction and a positive angle is in the clockwise direction). Figure 5 shows a schematic down-looking wind observation geometry and a swath of the SLAS-borne CDWL. The location of the laser footprint with a diameter of 2 m is determined by the combination of the nadir angle, azimuth angle, and orbital altitude; the laser footprint track is approximately 110 km away from the satellite ground track. The spacing between two laser footprints is determined by the ground track speed of the satellite and PRF. The Earth's rotation causes a successive satellite ground track spacing of 2370 km at 0° and 2030 km at 35° latitude. The ground track speed of the satellite is 7.5 km s^{-1}; a horizontal resolution of 100 km corresponds to approximately 13.3 s. The separation between a pair of orthogonal LOS wind is 12.8 s. The forward and backward laser directions are alternately switched.

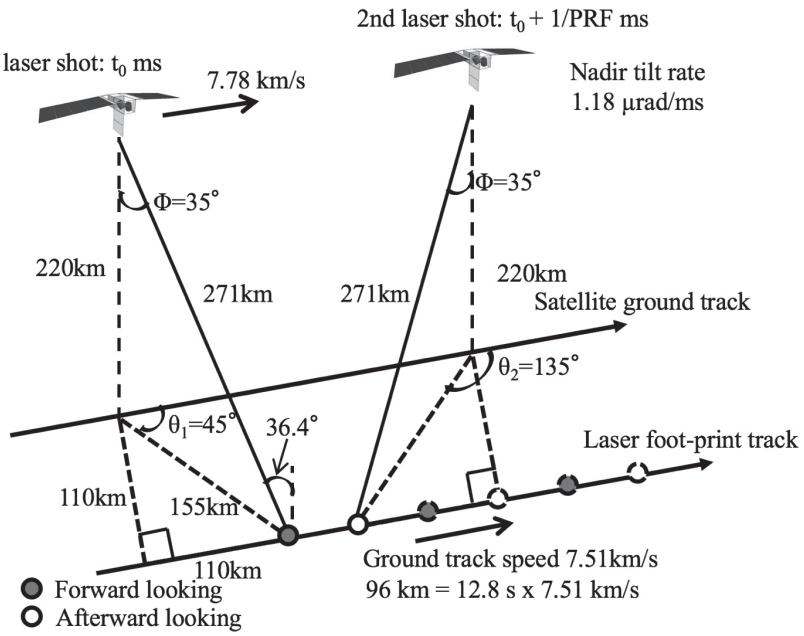

Fig. 5. Down-looking wind profile observation geometry of SLAS-borne CDWL using two telescopes.

4. Key technology required for space-borne coherent Doppler wind lidar

The power backscattered from the atmosphere decreases with the square of the range to the target atmosphere. The pulse energy of a laser required for an ISS JEM-CDL flying at 400 km altitude was 0.5 J (Ishii 2009, personal communication) at a PRF of 10 Hz. The low orbital altitude of the SLAS-borne CDWL allows the pulse energy of the laser of 0.5 J to be reduced fourfold (0.125 J). The average laser power required for the SLAS-borne CDWL is 1.25 W at 2 μm. NICT developed a 2-μm single-frequency Q-switched Tm, Ho: YLF laser operating at 30 Hz with a pulse duration of 150 ns_{FWHM} (FWHM: full width at half maximum) (Ishii et al. 2010; Mizutani et al. 2015). JAXA developed a 1.5-μm optical fiber laser for airborne application emitting 0.0019 J at 4000 Hz (average power = 7.6 W) (Inokuchi and Tanaka 2009; Inokuchi et al. 2014). Using Eqs. (3), (7), (14), and (17), average powers of 40 W and 15 W for Ångström exponent of 0.3 and 2 respectively are required at the 1.55-μm CDL with 0.01 J pulse energy to obtain the same LOS wind speed error dv as that of a 2-μm CDWL with 0.125 J pulse energy at 30 Hz. In this study, the designs for 1.5- and 2- μm lasers permit a pulse energy of 0.01 J and a PRF of 1500 (Ångström exponent = 2.0) to 4000 Hz (Ångström exponent = 0.3), and a pulse energy of 0.125 J and a PRF of 30 Hz, respectively. The pulse width for both lasers is 200 ns.

A CDWL requires a single-frequency Q-switched laser. A single-frequency Q-switched laser pulse is achieved by injection seeding with a single-frequency CW laser beam matched to a pulse laser by the ramp-and-fire technique (Henderson et al. 1986). The single-frequency CW laser is critical for the injection seeding and heterodyne detection. It is important to develop a reliable single-frequency CW laser for the future SLAS-borne CDWL. The single-frequency CW laser needs to have a small frequency jitter, which means that it does not change the frequency during the round-trip time between the CDWL and the target atmosphere. Technical requirements for the target 2-μm laser are the TEM_{00} mode, wavelength tuning, an output of > 30 mW, long power stability, linear polarization, and a frequency jitter of < 10 kHz m s^{-1}. Figure 6 shows two candidate laser systems for the 2-μm Q-switched pulse laser with a noncomposite Tm, Ho: YLF laser rod: (a) a one-oscillator configuration and (b) a master oscillator power amplifier (MOPA) configuration. For the current laser-diode-pumped (LD-pumped) 2-μm single-frequency Q-switched Tm, Ho: YLF laser developed at NICT, it has been experimentally shown that the average laser power increases at a rate of 0.1 W $°C^{-1}$ with the cooling of the laser

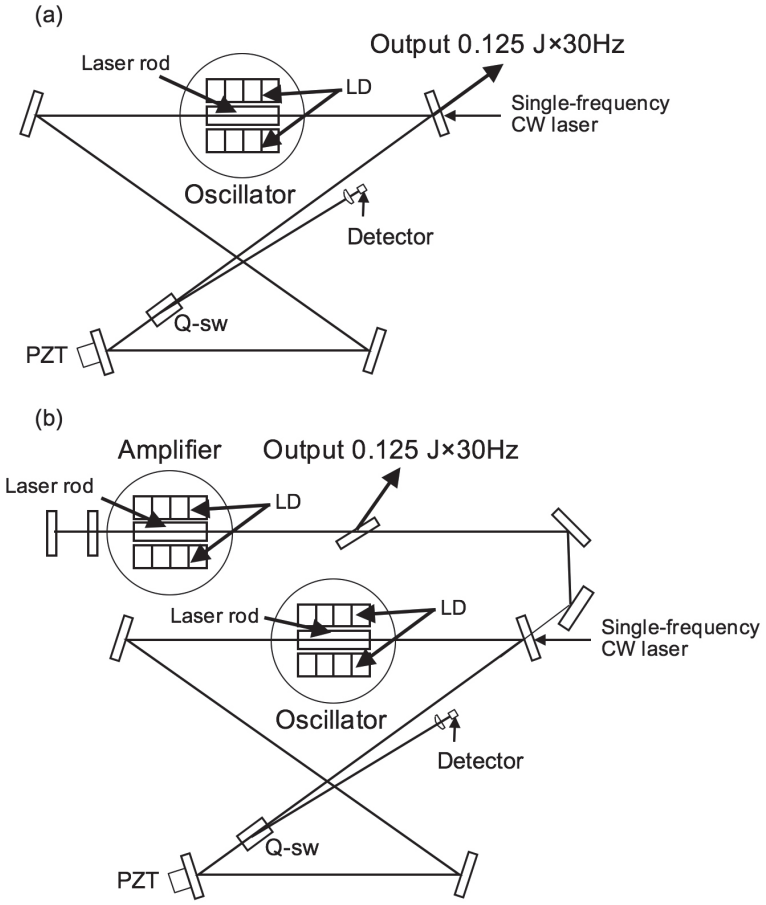

Fig. 6. Candidate 2-μm laser system configurations: (a) one-oscillator configuration and (b) master oscillator and amplifier configuration. A single-frequency CW laser is used for injection seeding. Q-sw is an optical component for Q-switching. PZT is a piezoelectric translator with a mirror for controlling the cavity length of the laser.

rod. The Tm, Ho: YLF laser rod should be cooled to lower than roughly −100 °C to achieve an average laser power of 3.75 W (0.125 J pulse^{-1}, 30 Hz). A cooling system would require a large amount of electrical power to cool the Tm, Ho: YLF laser rod to such a low temperature. The MOPA configuration is another approach because it is not necessary to cool the Tm, Ho: YLF laser rod to such a low temperature. We constructed a new laser model for the design of the Tm, Ho: YLF laser (Sato et al. 2014), which is a major improvement on previous laser models (e.g., Walsh et al. 2000). We are theoretically and experimentally investigating the feasibility of the MOPA-configured 2-μm laser operating at a laser rod temperature higher than −40 °C. Preliminary results of the simulation using the new laser model show the possibility that the MOPA-configured 2-μm laser could emit a laser pulse of 0.125 J at a PRF of 30 Hz. The MOPA-configured 2-μm laser could also use thermoelectric cooling systems for cooling two Tm, Ho: YLF lasers. We understand that the laser configuration has a trade-off between the laser power and the power required for heat removal and electrical power consumption. A high-power laser is the component with the highest risk in a lidar system. High-power laser diode arrays (LDAs) are used to pump a laser rod in the pumping laser module. NASA GSFC (2006) studied the reliability of LDAs for space-borne laser application and established guidelines for the qualification and screening testing of LDAs. Currently, another high risk for the space-qualified laser is laser-induced damage (LID) due to outgas from the adhesion material. Preventing LID requires special attention to the design of a high-pulse-energy laser system. We con-

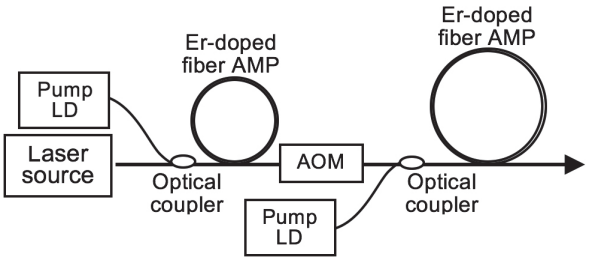

Fig. 7. The 1.5-μm laser system with erbium-doped optical fiber amplifier (Er-doped fiber AMP).

ducted destructive tests to evaluate the performances of various optical coatings at 2 μm and obtained the high-damage threshold for the 2-μm optics with ion-beam sputtering coating.

Figure 7 shows a candidate 1.5-μm optical fiber laser with the MOPA configuration. The 1.5-μm optical fiber laser comprises a small-power laser source, an AOM used for generating a pulse waveform, and erbium-doped optical fiber amplifiers. The 1.5-μm optical fiber applications rely on well-developed materials and well-established telecommunication devices. The technology of the 1.5-μm optical fiber laser has advantages for lidar applications, such as weight, size, robustness, and free optical alignment. However, there are also challenges in realizing a light source to meet the requirements of the future SLAS-borne CDWL: a high PRF (1500 to 4000 Hz), a single frequency, high-energy pulse (0.01 J), laser beam quality, the amplified spontaneous emission (ASE) effect, and polarization-maintaining operation. New glass rare-earth host materials will enable the development of a highly doped optical fiber amplifier with a short length and large mode area. A highly doped optical fiber amplifier produces high pulse energy. The high pulse energy indicates a nonlinear process in the optical fiber, especially for stimulated Brillouin scattering (SBS). The SBS restricts the input optical power, and it is a limiting factor for the achievable pulse energy. To reduce the nonlinearity of the process, a planar waveguide is being developed using glass rare-earth host materials. The planar waveguide laser has attractive features such as high efficiency, high beam quality, among other related features. To the best of our knowledge, the highest average power of an Er-doped fiber laser with a planar waveguide is 7.6 W with a pulse energy of 1.9 mJ and a pulse width of 580 ns (Sakimura et al. 2012). A laser pulse with a log pulse width has a narrow linewidth in the frequency domain. The narrow-linewidth laser pulse is useful for frequency analysis with a high-frequency resolution, leading to wind measurement with high precision. Sakimura et al. (2012) reported gain saturation due to the ASE effect. A 1.5-μm optical fiber laser with an average power of 10 W has not been demonstrated even at the laboratory level. Further technical studies are necessary to develop a 1.5-μm optical fiber laser meeting the requirements of the future SLAS-borne CDWL. The 2-μm laser technology for a space-borne lidar has been matured in Japan (Ishii et al. 2010; Mizutani et al. 2015; Sato et al. 2017). Therefore, the 2-μm laser is a better approach for the future SLAS-borne CDWL than the 1.5-μm laser system. Hereafter and in Part 2, we focus on the space-borne CDWL with a 2-μm laser.

A key requirement for a coherent receiver is a telescope with diffraction-limited performance. NICT has developed afocal telescopes for a 2-μm coherent lidar. The afocal telescopes have a two-mirror off-axis Mersenne design to minimize wavefront aberrations and have excellent wavefront accuracy. The afocal telescopes are coaxial systems with a beam-expanding collimator and a receiving telescope. We are accumulating knowledge and technologies to design and fabricate an afocal telescope with a large aperture. Since the motion of a scanning device causes scanning-induced momentum and affects the altitude determination and control of a satellite, the space-borne CDWL described in previous studies (Iwasaki 1999; Ishii 2009) uses two fixed off-axis telescopes with a 40-cm clear aperture. Reducing the mass and size of the mirror and telescope allows a longer operation by reducing the fuel consumption.

The SLAS will fly at a track speed of approximately 7.8 km s^{-1}. We assume that the SLAS track was parallel to Earth rotation direction. Earth rotation speed is approximately 460 m s^{-1}. For a wind speed of 100 m s^{-1} (i.e., the upper limit measurement requirement for the velocity) and Earth rotation speed of 460 m s^{-1}, the Doppler-shifted frequency at 2 μm is 8.4 GHz (= 7.8 + 0.1 + 0.5 GHz). The laser pulse will be sent into the atmosphere at azimuth angles of 45° and 135° and at a nadir angle of 35°. The Doppler-shifted frequency is about 3.4 GHz [= $8.4 \cdot \cos(45°)\sin(35°)$]. A detector with a bandwidth of > 3.4 GHz is necessary for the space-borne CDWL wind measurements. An InGaAs detector is one of the candidate detectors. The electrical characteristics of an InGaAs detector can be affected by proton radiation with increasing number of protons (Garden 2000). The InGaAs detector must be designed and fabricated in accordance with the orbital type and altitude of the SLAS, the mission duration

with respect to the solar activity, and the shielding of the SLAS. The Doppler-shifted frequency due to the satellite speed can be compensated by hardware-based onboard frequency calibration and down-converted to the IF frequency center of 100 MHz. Fluctuations in the frequency of the outgoing laser pulse due to short-term frequency drifting of the mechanical fluctuations of the piezoelectric translator (PZT) motion, long-term frequency drifting of the single-frequency CW laser, and other types of frequency drifting can be corrected by an algorithm proposed by Frehlich et al. (1997). Analog-to-digital (AD) conversion from an analog signal to a discrete signal is commonly used in data processing. Both the sampling frequency and the number of sampling points of an AD converter determine the frequency and range resolutions in DWL wind measurement. There are some space-qualified, high-speed, and high-resolution AD converters [e.g., Texas Instruments ADS5463-SP (12-bit resolution, 500 MHz sampling frequency) and ADS5474-SP (14-bit resolution, 400 MHz sampling frequency)]. The range and frequency resolutions are determined by the sampling frequency and the number of sampling points. The two resolutions have a trade-off relation with each other. To accurately investigate the uncertainty of wind measurement due to the frequency fluctuation in the outgoing laser pulse, different numbers of sampling points are used for frequency analysis. An AD converter with a high bit resolution is useful for estimating the power of the backscattered signal and retrieving the backscattering coefficient from the target atmosphere. In this study, we selected an AD converter with 14-bit resolution and 400 MHz sampling frequency. If 4096-point and 256-point FFTs are used for the frequency analysis of outgoing laser pulses and backscattered signals, the frequency resolutions for the 4096-point and 256-point FFTs are 0.10 and 1.56 MHz, respectively, and the 256-point FFT corresponds to a range resolution of 96 m. The space-qualified, high-speed, and high-resolution AD converters will be sufficient to meet the WMO observational user requirements (WMO 2015, http://www.wmo-sat.info/oscar/variables/view/179). The concept of the space-borne CDWL is summarized in Table 4.

Table 4. Summary of SLAS-borne CDWL.

Wavelength (μm)	2.05
Pulse energy (J)	0.125
Pulse duration (ns_{FWHM})	200
PRF (Hz)	30
Telescope diameter (m)	0.4
Number of laser directions	2
Detector quantum efficiency	0.8
Heterodyne efficiency	0.4
Optical efficiency	0.44
Unknown system efficiency	0.5
Sampling frequency (MHz)	400
Sampling points	256
Azimuth angle of observation direction (°)	45, 135
Nadir angle of observation direction (°)	35
Target horizontal resolution (km)	< 100
Target vertical resolution (km)	Altitude 0–3 km: < 0.5 Altitude 3–8 km: < 1 Altitude 8–20 km: < 2

5. Summary

Wind profile observation is important to improve NWP, climate studies, and various meteorological studies. Current space-borne observing systems are biased to temperature- and water-vapor-related measurements. The AMV can hardly retrieve vector wind with a high vertical resolution and precise height assignment. A space-borne DWL is a promising remote sensing technique for global wind profile observation and will solve the issues facing current space-borne observing systems. In this paper, we described the concept of a future space-borne CDWL. Our working group is studying the feasibility of a future Japanese space-borne CDWL from technical and scientific viewpoints. An instrumental overview of the space-borne DWL is described in this paper. The future mission concept described here will be the first space-borne DWL with heterodyne detection, and it is designed to have two LOSs for vector wind measurement from a new SLAS. The SLAS will be a challenging innovative technology for next-generation Earth observation satellites. There are two candidate orbits, 96.4° (a polar orbit similar to that of ADM-Aelous) and 35.1° (low-inclination-angle orbit similar to that of TRMM). The satellite orbit and altitude are under discussion from the scientific viewpoint. The CDWL uses an eye-safe transmitter with a single frequency, high pulse energy, and long pulse width. The development of a space-qualified single-frequency pulse laser will provide opportunities for future space-borne lidar such as high spectral resolution lidar or differential absorption lidar. Heterodyne detection is a challenging technique to be carried out under diffraction-limited and shot-noise-limited conditions. Heterodyne detection is a novel technique allowing daytime and nighttime wind measurements without

considering solar background noise. The technical requirements of the SLAS-borne CDWL are an average laser power of 3.75 W (0.125 J at a PRF of 30 Hz) at 2 μm, two effective 40-cm-diameter afocal telescopes, a wide-bandwidth (> 3.4 GHz) detector, a high-speed AD converter, and a systematic lidar efficiency of 0.08.

The SLAS-borne CDWL will provide a full vector wind profile with high vertical resolution, low bias, and high precision at along-track horizontal and vertical resolutions better than 100 km, and < 0.5 km for the altitude range of 0–3 km and < 1 km for the altitude range of 3–8 km, respectively, in the presence of moderate- or enhanced-loaded aerosol and cloud and it will fill the gap of the current global wind observing systems. Note that it is true when moderate- or enhanced-loaded aerosol and cloud are present. By providing global wind profiling and intercalibration between the SLAS-borne CDWL and other global wind observing systems, the SLAS-borne CDWL will be complementary and offer insights into the improvement and development of algorithms for passive sensors. Synergistic wind measurements using the SLAS-borne CDWL and other global wind observing systems should improve the initial conditions for NWP; the prediction of typhoons, heavy rain, and atmospheric transport; and meteorological studies.

Acknowledgments

The authors would like to thank the anonymous reviewers for their valuable comments and suggestions to improve the quality of the paper. The authors wish to thank Tatemasa Miyoshi of the RIKEN Advanced Institute for Computational Science; Masakatsu Nakajima, Hamaki Inokuchi, Maki Hirakata, and Hirokazu Hoshino of JAXA; Kazuhiro Asai of Tokyo Institute of Technology; and Kazumasa Aonashi of JMA/MRI for supporting the research activity of the working group. The authors wish to thank Yoshiaki Sato of JMA; Munehiko Yamaguchi of JMA/MRI; Fumio Hasebe of Hokkaido University; Hirohiko Masunaga of Nagoya University; Masato Shiotani, Tetsuya Takemi, and Eriko Nishimoto of Kyoto University; Yasukuni Shibata of Tokyo Metropolitan University; and Tetsuo Shina of Chiba University for contributing to the implementation plan for the future space-borne DWL in Japan and supporting the research activity of the working group. The authors thank the GPM Utilization Committee for supporting the working group. The authors wish to thank Toshikazu Itabe for many useful discussions and helpful advice.

A part of this research was supported by JSPS KAKENHI under Grant Numbers 15K06129 and 15K05293.

References

Ångström, A., 1964: The parameters of atmospheric turbidity. *Tellus*, **16**, 64–75.

Atlas, R., L. Bucci, B. Annane, R. N. Hoffman, and S. T. Murillo, 2015a: Observing system simulation experiments to assess the potential impact of new observing systems on hurricane forecasting. *Mar. Technol. Soc. J.*, **49**, 140–148.

Atlas, R., R. N. Hoffman, Z. Ma, G. D. Emmitt, S. A. Wood, Jr., S. Greco, S. Tucker, L. Bucci, B. Annane, R. M. Hardesty, and S. Murillo, 2015b: Observing system simulation experiments (OSSEs) to evaluate the potential impact of an optical autocovariance wind lidar (OAWL) on Numerical Weather Prediction. *J. Atmos. Oceanic Technol.*, **32**, 1593–1613.

Baker, W. E., R. Atlas, C. Cardinali, A. Clement, G. D. Emmitt, B. M. Gentry, R. M. Hardesty, E. Källén, M. J. Kavaya, R. Langland, Z. Ma, M. Masutani, W. McCarty, R. Bradley Pierce, Z. Pu, L. P. Riishøjgaard, J. Ryan, S. Tucker, M. Weissmann, and J. G. Yoe, 2014: Lidar-measured wind profiles: The missing link in the global observing system. *Bull. Amer. Meteor. Soc.*, **95**, 543–564.

Baron, P., S. Ishii, K. Okamoto, K. Gamo, K. Mizutani, C. Takahashi, T. Itabe, T. Iwasaki, T. Kubota, T. Maki, R. Oki, S. Ochiai, D. Sakaizawa, M. Satoh, Y. Satoh, T. Y. Tanaka, and M. Yasui, 2017: Feasibility study for future space-borne coherent Doppler wind lidar, Part 2: Measurement simulation algorithms and retrieval error characterization. *J. Meteor. Soc. Japan*, **95**, 319–342.

Bilbro, J., R. Beranek, D. Fitzjarrald, and J. Mabry, 1987: *Shuttle Coherent Atmospheric Lidar Experiment*. NASA Tech. Memo., NASA TM-100307, 280 pp. [Available at https://ntrs.nasa.gov/archive/nasa/casi.ntrs.nasa.gov/19870014526.pdf.]

Bowdle, D. A., J. Rothermel, J. E. Arnold, and F. S. Williams, 1991: GLObal Backscatter Experiment (GLOBE) Pacific survey mission. *NASA, Washington, 4th Airborne Geoscience Workshop*, US, 107–110. [Available at https://ntrs.nasa.gov/archive/nasa/casi.ntrs.nasa.gov/19910016138.pdf.]

Emmitt, G. D., 2001: Hybrid technology Doppler wind lidar: Assessment of simulated data products for a space-based system concept. *Proc. SPIE*, **4153**, 366–375.

ESA, 1999: *Atmospheric Dynamics Mission*. The Four Candidate Earth Explorer Core Missions. Mission Selection Rep. ESA SP-1233(4), 129 pp.

ESA, 2001: *ADM-Aeolus Project System Requirements Document for Phases B, C/D, E1*. AE-RS-ESA-SY-001, 17, ESTEC, 49 pp.

Folger, K., and M. Weissmann, 2014: Height correction of atmospheric motion vectors using satellite lidar obser-

vations from CALIPSO. *J. Appl. Meteor. Climatol.*, **53**, 1809–1819.

Frehlich, R., 2004: Velocity error for coherent Doppler lidar with pulse accumulation. *J. Atmos. Oceanic Technol.*, **21**, 905–919.

Frehlich, R. G., and M. J. Kavaya, 1991: Coherent laser radar performance for general atmospheric refractive turbulence. *Appl. Opt.*, **30**, 5325–5352.

Frehlich, R. G., and M. J. Yadlowsky, 1994: Performance of mean-frequency estimators for Doppler radar and lidar. *J. Atmos. Oceanic Technol.*, **11**, 1217–1230.

Frehlich, R., S. M. Hannon, and S. W. Henderson, 1997: Coherent Doppler lidar measurements of winds in the weak signal regime. *Appl. Opt.*, **36**, 3491–3499.

Garden, C., 2000: *Effects of proton radiation on InGaAs photodiodes and laser diodes*. ESTEC Working Paper EWP-2117. [Available at https://escies.org/download/webDocumentFile?id=944.]

Grund, C. J., J. Howell, R. Pierce, and M. Stephens, 2009: Optical autocovariance direct detection lidar for simultaneous wind, aerosol, and chemistry profiling from ground, air, and space platforms. *Proc. SPIE*, **7312**, 73120U, doi:10.1117/12.824204.

Hardesty, M., B. Gentry, W. Baker, D. Emmitt, M. Kavaya, S. Mango, and K. Miller, 2011: *The Winds from the International Space Station for Climate Research (WISSCR) Mission*. [Available at http://cires1.colorado.edu/events/lidarworkshop/LWG/Feb11/LWGPapers.feb11/Hardesty.feb11.pptx.]

Hayashi, M., and K. Shimoji, 2013: *Atmospheric motion vectors derivation algorithm*. Meteorological satellite center technical note, **58**, 109 pp (in Japanese).

Henderson, S. W., E. H. Yuen, and E. S. Fry, 1986: Fast resonance-detection technique for single-frequency operation of injection-seeded Nd:YAG lasers. *Opt. Lett.*, **11**, 715–717.

Huffaker, R. M., 1978: *Feasibility study of satellite-borne lidar global wind monitoring system*. NOAA Tech. Memo., ERL WPL-37, 276 pp.

Huffaker, R. M., T. R. Lawrence, R. J. Keeler, M. J. Post, J. T. Priestley, and J. A. Korrell, 1980: *Feasibility study of satellite-borne lidar global wind monitoring system, Part II*. NOAA Tech. Memo., ERL WPL-63, 124 pp.

Huffaker, R. M., T. R. Lawrence, M. J. Post, J. T. Priestley, F. F. Hall, R. A. Richter, and R. J. Keeler, 1984: Feasibility studies for a global wind measuring satellite system (Windsat): Analysis of simulated performance. *Appl. Opt.*, **23**, 2523–2536.

Inokuchi, H., H. Tanaka, and T. Ando, 2009: Development of an onboard Doppler lidar for flight safety. *J. Aircr.*, **46**, 1411–1415.

Inokuchi, H., M. Furuta, and T. Inagaki, 2014: High altitude demonstration flights on an airborne Doppler lidar. *J. Japan Soc. Aeronaut. Spac. Sci.*, **62**, 198–203.

Ishibashi, T., 2014: Observing system simulation experiments with multiple methods. *Proc. SPIE*, **9265**, 926508, doi:10.1117/12.2069087.

Ishii, S., K. Mizutani, H. Fukuoka, T. Ishikawa, P. Baron, H. Iwai, T. Aoki, T. Itabe, A. Sato, and K. Asai, 2010: Coherent 2-μm differential absorption and wind lidar with conductively-cooled laser and two-axis scanning device. *Appl. Opt.*, **49**, 1809–1817.

Ishii, S., K. Okamoto, P. Baron, T. Kubota, Y. Satoh, D. Sakaizawa, T. Ishibashi, T. Y. Tanaka, K. Yamashita, S. Ochiai, K. Gamo, M. Yasui, R. Oki, M. Satoh, and T. Iwasaki, 2016: Measurement performance assessment of future space-borne Doppler wind lidar for Numerical Weather Prediction. *SOLA*, **12**, 55–59.

Iwai, H., S. Ishii, R. Oda, K. Mizutani, S. Sekizawa, and Y. Murayama, 2013: Performance and technique of coherent 2-μm differential absorption and wind lidar for wind measurement. *J. Atmos. Oceanic Technol.*, **30**, 429–449.

Iwasaki, T., and Coherent Doppler lidar sub group, 1999: *Science plan for ISS-borne coherent Doppler wind lidar measurement*. Advanced Earth Science and Technology Organization, 107 pp (in Japanese).

Kavaya, M. J., and G. D. Emmitt, 1998: Space Readiness Coherent Lidar Experiment (SPARCLE) space shuttle mission. *Proc. SPIE*, **3380**, doi:10.1117/12.327186.

Marseille, G.-J., A. Stoffelen, and J. Barkmeitjer, 2008: Sensitivity observing system experiment (SOSE)—A new effective NWP-based tool in designing the global observing system. *Tellus A*, **60**, 216–233.

Masutani, M., J. S. Woollen, S. J. Lord, G. D. Emmitt, T. J. Kleespies, S. A. Wood, S. Greco, H. Sun, J. Terry, V. Kapoor, R. Treadon, and K. A. Campana, 2010: Observing system simulation experiments at the National Centers for Environmental Prediction. *J. Geophys. Res.*, **115**, D07101, doi:10.1029/2009JD012528.

Menzies, R. T., 1986: Doppler lidar atmospheric wind sensors: A comparative performance evaluation for global measurement applications from earth orbit. *Appl. Opt.*, **25**, 2546–2553.

Mizutani, K., T. Itabe, S. Ishii, M. Aoki, K. Asai, A. Sato, H. Fukuoka, T. Ishikawa, and K. Noda, 2015: Diode-pumped 2-μm pulse laser with noncomposite Tm, Ho: YLF rod conduction-cooled down to −80°C. *Appl. Opt.*, **54**, 7865–7869.

NASA, 1989: *Laser Atmospheric Wind Sounder*. Earth Observing System, Instrument Panel Report. **IIg**, 55 pp. [Available at https://ntrs.nasa.gov/archive/nasa/casi.ntrs.nasa.gov/19890002787.pdf.]

NASA GSFC, 2006: *High power laser diode array qualification and guidelines for space flight environments*. NASA Parts and Packageing Program, 44 pp. [Available at http://ntrs.nasa.gov/archive/nasa/casi.ntrs.nasa.gov/ 20070021407.pdf.]

National Research Council, 2007: A Community assessment and strategy for the future. *Earth Science and Applications from Space: National Imperatives for the Next Decade and Beyond*. The National Academic Press,

311–317.

Noda, A., M. Homma, and M. Utashima, 2009: The study of a super low altitude satellite. *Trans. JSASS Space Tech. Japan*, **7**, Pf17–Pf22.

Okamoto, K., S. Ishii, P. Baron, T. Ishibashi, and T. Tanaka, 2017: Feasibility study for future Space-Borne Coherent Doppler Wind Lidar, Part 3: Initial evaluation using the operational global data assimilation system. *J. Meteor. Soc. Japan*., submitted.

Otsuka, M., M. Kunii, H. Seko, K. Shimoji, M. Hayashi, and K. Yamashita, 2015: Assimilation experiments of MTSAT rapid scan atmospheric motion vectors on a heavy rainfall event. *J. Meteor. Soc. Japan*, **93**, 459–475.

Petheram, J. C., G. Frohbeiter, and A. Rosenberg, 1989: Carbon dioxide Doppler lidar wind sensor on a space station polar platform. *Appl. Opt.*, **28**, 834–839.

Riishøjgaard, L. P., R. Atlas, and G. D. Emmitt, 2004: The impact of Doppler lidar wind observations on a single-level meteorological analysis. *J. Appl. Meteor.*, **43**, 810–820.

Rye, B. J., 1979: Antenna parameters for incoherent backscatter heterodyne lidar. *Appl. Opt.*, **18**, 1390–1398.

Rye, B. J., and R. M. Hardesty, 1993: Discrete spectral peak estimation in incoherent backscatter heterodyne lidar. I. Spectral accumulation and the Cramer–Rao lower bound. *IEEE Trans. Geosci. Remote Sens.*, **31**, 16–27.

Sakimura, T., Y. Watanabe, T. Ando, S. Kameyama, K. Asaka, H. Tanaka, T. Yanagisawa, Y. Hirano, and H. Inokuchi, 2012: 1.5-μm high average power laser amplifier using an Er,Yb:Glass planar waveguide for coherent Doppler lidar. *Proc. SPIE*, **8526**, doi:10.1117/12.976293.

Sato, A., K. Asai, Y. Miyake, S. Ishii, K. Mizutani, and S. Ochiai, 2014: A design strategy for a high-energy Tm, Ho: YLF laser transmitter. *Proc. SPIE*, **9262**, doi:10.1117/12.2069367.

Sato, A., M. Aoki, S. Ishii, R. Otsuka, K. Mizutani, and S. Ochiai, 2017: 7.28-W, high-energy, conductively cooled, Q-switched Tm, Ho: YLF laser. *IEEE Photonics Technol. Lett.*, **29**, 134–137.

Scharf, L. L., 1991: Maximum Likelihood Estimators. *Statistical Signal Processing*. Addison-Wesley, 221–235.

Seinfeld, J. H., and S. N. Pandis, 1988: Thermodynamics of Aerosols. *Atmospheric Chemistry and Physics*. Wiley-Interscience Publication, New York, US, 429–446.

Srivastava, V., J. Rothermel, A. D. Clarke, J. D. Spinhirne, R. T. Menzies, D. R. Cutten, M. A. Jarzembski, D. A. Bowdle, and E. W. McCaul, 2001: Wavelength dependence of backscatter by use of aerosol microphysics and lidar data sets: application to 2.1-μm wavelength for space-based and airborne lidars. *Appl. Opt.*, **40**, 4759–4769.

Stoffelen, A., J. Pailleux, E. Källén, M. J. Vaughan, L. Isaksen, P. Flamant, W. Wergen, E. Andersson, H. Schyberg, A. Culoma, R. Meynart, M. Endemann, and P. Ingmann, 2005: The Atmospheric Dynamics Mission for global wind field measurement. *Bull. Amer. Meteor. Soc.*, **86**, 73–87.

Tucker, S., and C. Weimer, 2014: ATHENA-OAWL: Instrument overview. *In 2014 spring meeting of Working Group on Space-based Lidar Winds*, 14 May 2014, Colorado, US. [Available at http://cires1.colorado.edu/events/lidarworkshop/LWG/May14/presentations/Tucker_ATHENA-OAWL%20Instrument%20Overview.pdf.]

Velden, C. S., and K. M. Bedka, 2009: Identifying the uncertainty in determining satellite-derived atmospheric motion vector height attribution. *J. Appl. Meteor. Climatol.*, **48**, 450–463.

Walsh, B. M., N. P. Barnes, and B. D. Bartolo, 2000: The temperature dependence of energy transfer between the Tm $^3F_4$ and Ho $^5I_7$ manifolds of Tm-sensitized Ho luminescence in YAG and YLF. *J. Lumin.*, **90**, 39–48.

WMO, 2012: *WMO Integrated Global Observing System; Final report of the Fifth WMO Workshop on the Impact of Various Observing Systems on Numerical Weather Prediction*. WMO Tech. Rep. 2012-1, 6.

Zrnic, D. S., 1979: Estimation of spectral moments for weather echoes. *IEEE Trans. Geosci. Electron.*, **17**, 113–128.